

Piezoelectric composite frequency steerable acoustic transducers for impact monitoring

Shulong Zhou¹ , Yanfeng Shen¹ , Chunquan Wang²,
 Bao Wang² and Yuan Tian²

Structural Health Monitoring
 1–17

© The Author(s) 2025

Article reuse guidelines:

sagepub.com/journals-permissions

DOI: 10.1177/14759217251343880

journals.sagepub.com/home/shm



Abstract

This paper presents a novel piezoelectric composite frequency steerable acoustic transducers (PC-FSATs) for impact monitoring. Unlike conventional impact monitoring systems, which generally demand dense sensor networks and complex detection algorithms, PC-FSATs utilize merely two channels for achieving large-area monitoring, rendering significant system simplification and cost reduction. The PC-FSATs leverage the frequency-dependent spatial filtering mechanism, establishing a direct correlation between the elastic wave propagation direction and the frequency content of the received signal. By identifying the frequency components of the incident wave, the impact orientation can be accurately evaluated. The proposed PC-FSAT is comprised of flexible printed circuits with embedded, radially oriented piezoceramic fibers sandwiched within the central layers, which augments the transducer's directional sensitivity while imparting favorable sensor flexibility. This research initiates with the analytical formulation of the frequency-wavenumber beam steering mechanism for the transducer design. Subsequently, finite element simulations are carried out to demonstrate the impact detection principle. Furthermore, impact monitoring and localization experiments are performed on a drop-ball platform. The results demonstrate that the proposed system can accurately locate the impact event with only a pair of transducers. This novel transducer offers a promising solution for the development of cost-effective, reliable, and versatile impact monitoring systems, with potential applications in industries such as aerospace, automotive, and civil engineering. The paper finishes with summary, concluding remarks, and suggestions for future work.

Keywords

Frequency wavenumber, piezoelectric composite transducer, ultrasonic guided waves, impact monitoring, directional wave sensing

Introduction

Structural health monitoring (SHM) technology plays an essential role for ensuring the safety, reliability, and longevity of critical infrastructures by enabling the early identification of potential damage and preventing catastrophic failures. Among prevailing techniques, impact monitoring is a key aspect in SHM, aiming at detecting anomalous external intrusive events such as mechanical collisions and accidental falls.^{1,2} Prompt and accurate identification of impacts is crucial for minimizing downtime, reducing maintenance costs, and safeguarding structural integrity. In this context, guided-wave-based methods have become a prominent approach due to their ability to propagate over long distances with minimal amplitude attenuation, as well as their high sensitivity to structural defects.^{3–8}

Guided-wave-based impact monitoring methods typically rely on passive recordings, where ultrasonic guided waves, generated by an impact event, propagate omnidirectionally and are captured by multiple sensors distributed across the structure. These waves contain critical information about the impact's location, orientation, and severity, which can be extracted through signal processing and data interpretation. Researchers

¹University of Michigan-Shanghai Jiao Tong University Joint Institute, Shanghai Jiao Tong University, Shanghai, China

²Wuxi City Huifeng Electronic. Co. Ltd, Wuxi, China

Corresponding author:

Yanfeng Shen, University of Michigan-Shanghai Jiao Tong University Joint Institute, Shanghai Jiao Tong University, Room 400C Longbin Building, Dongchuan Rd., Minhang, Shanghai 200240, China.

Email: yanfeng.shen@sjtu.edu.cn

have proposed various approaches to enhancing detection accuracy and coverage. Giurgiutiu et al.⁹ applied guided wave phased arrays using linear PZT (lead zirconate titanate) arrays for precise impact detection in composite structures. Giridhara et al.¹⁰ performed data fusion of multiple sensor arrays to augment the precision of impact diagnosis outcomes. Yuan et al.¹¹ proposed a wireless sensor network based on multi-response for large-scale impact monitoring, aiming at reducing system complexity and weight. Capineri et al.¹² quantitatively evaluated impact location errors through the Lamb wave guided mode S_0 . Although effective, these methods demand multiple-channel, dense sensor arrays to capture temporal waveforms at various locations, often necessitating complex wiring and advanced data acquisition hardware.

To address these issues, researchers have taken additional routes and explored advanced algorithms to improve impact detection, including deep learning and convolutional neural networks (CNNs). Zheng and Yuan¹³ analyzed different time delay acquisition methods for verifying the impact detection precision of the signal classification (MUSIC) algorithm. Feng et al.¹⁴ achieved accurate impact localization through merely four sensors in conjunction with a convolutional neural network. Zhu et al.¹⁵ combined the flexible piezoelectric sensor array with the MUSIC-assisted artificial intelligence network (ANN) algorithm to monitor structural impacts in a region of more than 7500% of its sensor implementation area. These approaches effectively reduce the number of sensors and mitigate limitations associated with manual feature selection. However, these methods face challenges such as requiring large datasets for training, complex data interpretation, and high computational costs, which limit their versatile and practical implementation in resource-constrained environments.

Pioneer research endeavors strive to overcome these limitations by introducing novel transducers with guided wave manipulation capabilities. For instance, Matt and Lanza di Scalea¹⁶ proposed a method using macro-fiber composite (MFC) piezoelectric rosettes to determine the orientation of incoming ultrasonic waves for impact localization in complex anisotropic structures. Laude et al.¹⁷ demonstrated the use of an annular interdigital transducer (AIDT) to achieve subwavelength focusing of surface acoustic waves on lithium niobate. Wang et al.¹⁸ developed a micromachined piezoelectric ultrasonic transducer (pMUT) to enhance the guided wave generation and reception sensitivity and directivity. On the other hand, frequency control has been shown to provide directional guidance for guided waves, enabling more efficient structural

monitoring solutions. Romanoni et al.¹⁹ investigated two-dimensional periodic piezoelectric actuators for SHM, demonstrating that simultaneous activation of the actuator array can achieve frequency-based beam steering and directional scanning capabilities. Senesi et al.²⁰ experimentally characterized a novel periodic frequency-steerable array to achieve guided wave beam steering and mode tuning of guided waves. Baravelli et al.²¹ proposed a double-channel frequency-steerable acoustic transducer (FSAT) with two-dimensional imaging capabilities for guided wave inspection, utilizing a spiral spatial distribution in wavenumber space to enable arbitrary beam steering and effective damage localization. Senesi and Ruzzene^{22–24} further developed the FSAT fabricated by PVDF and PZT for directional guided waves generation and reception on an aluminum plate. Nevertheless, the FSAT exhibited limited performance attributed to the omnidirectional piezoelectric coupling coefficients and unsatisfactory directionality constrained by conventional piezoelectric materials.²⁵ Recently, Mohammadgholiha et al.^{26–28} further developed the piezoceramic FSAT by patterning spiral electrodes onto a piezoelectric ceramic plate to complete SHM applications. However, endeavors on further enhancing the transducer directionality from the perspective of material design has not been reported. Moreover, these existing transducer designs inevitably suffer from the inherent brittleness of piezoceramics, which makes them prone to breakage during handling and bonding, especially for curved structural surfaces.

To overcome these challenges, this paper reports a novel piezoelectric composite transducer for enhanced directional guided wave sensing and impact monitoring. By embedding piezoceramic fibers within flexible printed circuits, the proposed transducers can overcome the brittleness of traditional piezoceramic FSATs. Radially configured piezoelectric fibers further elevate the directional sensitivity. This innovative design enables the transducers to conform to curved surfaces, significantly broadening their applicability in complex structural environments. Additionally, the use of frequency-wavenumber beam steering via featured piezo fiber alignment could achieve sensitivity selection of guided waves in distinct directions, reducing reliance on dense sensor arrays and simplifying data processing requirements. As a result, this approach offers a more efficient, cost-effective, and adaptive solution for impact monitoring on aerospace, automotive, and civil engineering industries, capable of addressing the limitations of existing technologies while maintaining high precision and reliability.

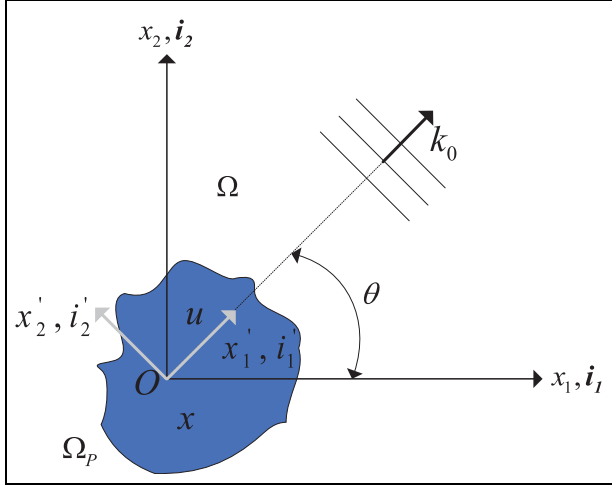


Figure 1. Schematic of wave propagating on the plane of the structure x (after Senesi et al.²²).

PC-FSATs: analytical formulation and pattern design

This section presents the analytical formulation for sensing guided waves with surface-mounted sensors, laying the foundation for understanding directional wave probing. It then introduces the design principle of the spiral electrode pattern, highlighting how frequency-wavenumber-based beam steering enables directional control of guided waves. Finally, the technical details of the piezoelectric composite transducer are discussed, including the integration of piezoceramic fibers within flexible printed circuits to improve durability and maintain high directional sensitivity.

Frequency-based sensing directivity concept

The frequency-based directivity design approach initiates with the analysis of voltage measurements from a piezoelectric patch with an arbitrary shape bonded on a plate structure, under constant charge conditions, as shown in Figure 1.

The voltage response can be modeled using the stress-charge formulation of the piezoelectric constitutive equations²²:

$$V_P = \frac{t_P}{E_{33}^e A_P} \mathbf{b}^T \int_{\Omega_P} \varepsilon dx_1 dx_2 \quad (1)$$

where, ε denotes the vector representing the in-plane strain components, and e represents the piezoelectric coupling matrix under constant stress conditions, which exhibits distinct directional characteristics in this study. Additionally, E_{33}^e refers to the piezoelectric permittivity at constant strain, t_P represents the patch

thickness, and A_P denotes the electrode area. The vector \mathbf{b} enables the selection of the polarization direction. In this case, it is set to $\mathbf{b} = [0 \ 0 \ 1]^T$ and assumed to be oriented across the thickness of the patch.²⁹

To evaluate the sensing voltage in the presence of a propagating plane wave, the surface displacement can in general be expressed as:

$$\mathbf{u}(\mathbf{x}, \omega) = U_0(\omega) e^{-jk_0(\omega) \cdot \mathbf{x}} \quad (2)$$

Where U_0 defines the amplitude of the wave at the considered frequency ω , and $\mathbf{k}_0(\omega) = k_0(\omega)(\cos\theta \mathbf{i}_1 + \sin\theta \mathbf{i}_2)$ is the considered wave vector defining plane wave propagation at an angle θ . The \mathbf{i}_1 and \mathbf{i}_2 are defined as the unit vectors as shown in Figure 1. Then the strain vector can be expressed as followed²²:

$$\varepsilon = \varepsilon_{1'1'} \mathbf{r}(\theta) = \frac{du_{1'}}{dx_1} \mathbf{r}(\theta) = jU_{1'0}(\omega) k_0(\omega) e^{-jk_0(\omega) \cdot \mathbf{x}'} \cdot \mathbf{r}(\theta) \quad (3)$$

where $U_{1'0}(\omega)$ stands for the amplitude of the wave traveling within the plane of the structure along the direction $\mathbf{r}(\theta) = [\cos^2(\theta), \sin^2(\theta), 0]^T$. Substituting Equation (3) into Equation (1) yields:

$$V_P(\omega) = jU_{1'0}(\omega) k_0(\omega) H(\theta) D_P(\omega, \theta) \quad (4)$$

The quantity H specifies the material properties of the piezo-structure system:

$$H(\theta) = \frac{t_P \mathbf{b}^T \mathbf{e} \mathbf{r}(\theta)}{A_P \epsilon_{33}^e} \quad (5)$$

and

$$D_P(\omega, \theta) = \int_{\Omega_P} e^{-jk_0(\omega) \cdot \mathbf{x}} f(\mathbf{x}) d\mathbf{x} \quad (6)$$

The parameter D_P characterizes the influence of the material distribution, as defined by the function $f(\mathbf{x})$. This formulation offers the flexibility to tailor the material and polarization distributions, enabling precise tuning of the sensor to specific wavelengths and corresponding wave modes, thereby facilitating the achievement of desired directional properties.

Transducer design in frequency wavenumber domain

The frequency-dependent directivity described in Equation (6) opens up the possibility of customizing the material distribution to achieve a desired directional response at specific frequencies. This design approach aims to create a directivity pattern where the frequency corresponding to maximum sensitivity is uniquely linked to the direction of wave propagation.

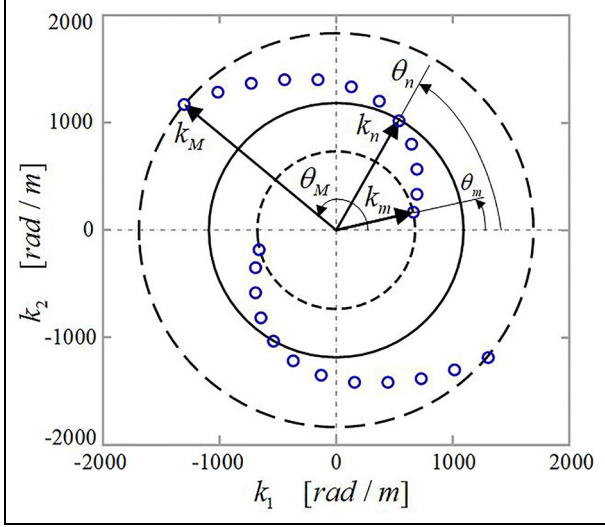


Figure 2. Schematic of spiral directivity in the wavenumber domain (after Senesi and Ruzzene²⁴). PC-FSAT: piezoelectric composite frequency steerable acoustic transducer.

A schematic representation of the desired wavenumber directivity is illustrated in Figure 2, where the locations of the directivity maxima trace a spiral path within the wavenumber space. The diagram shows a load distribution within a specified area from θ_m to θ_M with three iso-frequency circles. Each circle's radius corresponds to a particular wavenumber, and the increase in wavenumber leads to radiation occurring at progressively angles θ_n . Notably, the spiral configuration is achieved by selecting angular values such that the amplitude peaks are evenly spaced along the spiral path. This ensures that the transducer's response is designed to be highly directional at the specified frequencies, enabling precise control over the radiation pattern for various applications.

The spiral directivity function may be expressed as follows:

$$D_P(\mathbf{k}_0(\omega), \theta) = -j \frac{a}{N} \sum_{n=1}^N \left[\frac{J_1(a|\mathbf{k}_0 - \mathbf{k}_n|)}{a|\mathbf{k}_0 - \mathbf{k}_n|} - \frac{J_1(a|\mathbf{k}_0 + \mathbf{k}_n|)}{a|\mathbf{k}_0 + \mathbf{k}_n|} \right] \quad (7)$$

where a represents the radius of the patch in the spatial domain, while $J_1(x)$ denotes the first-order Bessel function. The wave vector \mathbf{k}_n corresponds to the angle θ_n at which the n -th maximum of the spiral is positioned, and where the associated directional lobe is observed. The location of \mathbf{k}_n as a function of θ_n is given by:

$$\mathbf{k}_n(\theta_n) = \left[(k_M - k_m) \frac{\theta_n - \theta_m}{\theta_M - \theta_m} + k_m \right] (\cos \theta_n \mathbf{i}_1 + \sin \theta_n \mathbf{i}_2) \quad (8)$$

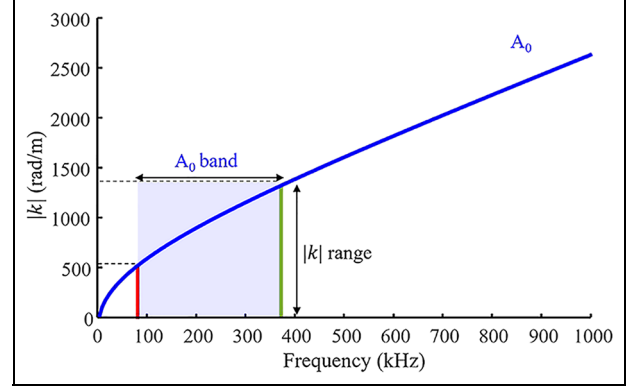


Figure 3. Dispersion curve for A_0 mode Lamb wave in a 1-mm thick aluminum plate.

This configuration represents the shape of an Archimedean spiral, where the amplitude of the wave vector varies between a minimum value k_m and a maximum value k_M . The spatial distribution of the sensing material is described by the following expression:

$$f(\mathbf{x}) = \frac{1}{N} \text{rect}\left(\frac{|\mathbf{x}|}{a}\right) \sum_{n=1}^N \sin(\mathbf{k}_n \cdot \mathbf{x}) \quad (9)$$

The dispersion relation analysis is employed to determine the excitation frequency of the transducer $f_{n,m}$ corresponding to the given wavenumber $k_{n,m}$, as depicted in Figure 3. It is crucial to highlight that the wavenumber distribution used in the design of the proposed transducer is specifically chosen to sense only the A_0 mode of the medium under consideration.

The design methodology for the proposed transducer is illustrated in Figure 4. As depicted in Figure 4(a), the design begins with defining the response distribution in the wavenumber domain. This is followed by obtaining the spatial distribution through the inverse Fourier transform (IFT) of the wavenumber domain into spatial domain, as depicted in Figure 4(b). It is important to note that the spatial distribution derived from Equation (9) may not be physically realizable, as it requires continuous material or polarization grading. To address this issue, a thresholding approach is applied. An effective method to overcome this limitation is to employ a three-level quantization of the spatial pattern distribution $f(\mathbf{x})$, employing a specific threshold as outlined in the following steps:

$$\bar{f}(\mathbf{x}) = \begin{cases} 1, & f(\mathbf{x}) \geq \eta \\ 0, & f(\mathbf{x}) \leq |\eta| \\ -1, & f(\mathbf{x}) \leq -\eta \end{cases} \quad (10)$$

The thresholding process effectively converts $f(\mathbf{x})$ into a function $\bar{f}(\mathbf{x})$ with a constant value distributed over

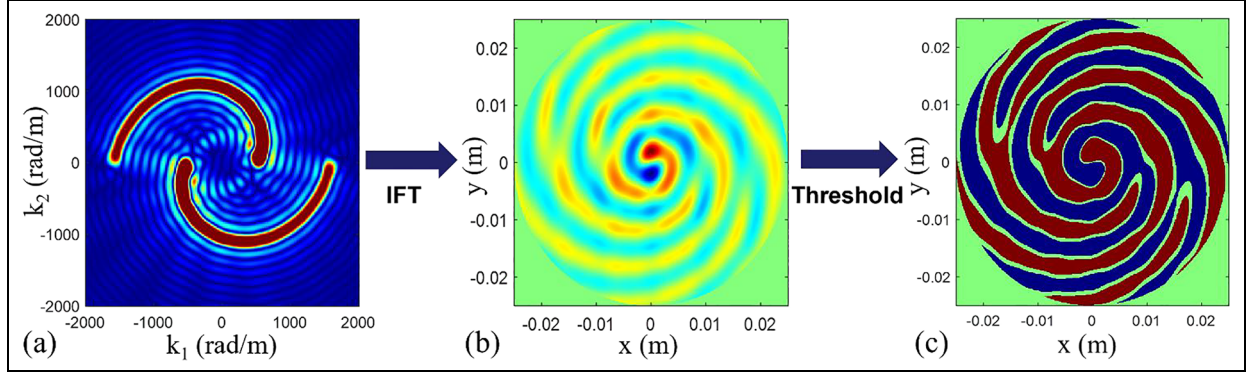


Figure 4. PC-FSATs design procedure: (a) wavenumber representation, (b) corresponding continuous spatial pattern, and (c) final spiral electrodes shape ($\eta = 7\%$).

PC-FSAT: piezoelectric composite frequency steerable acoustic transducer.

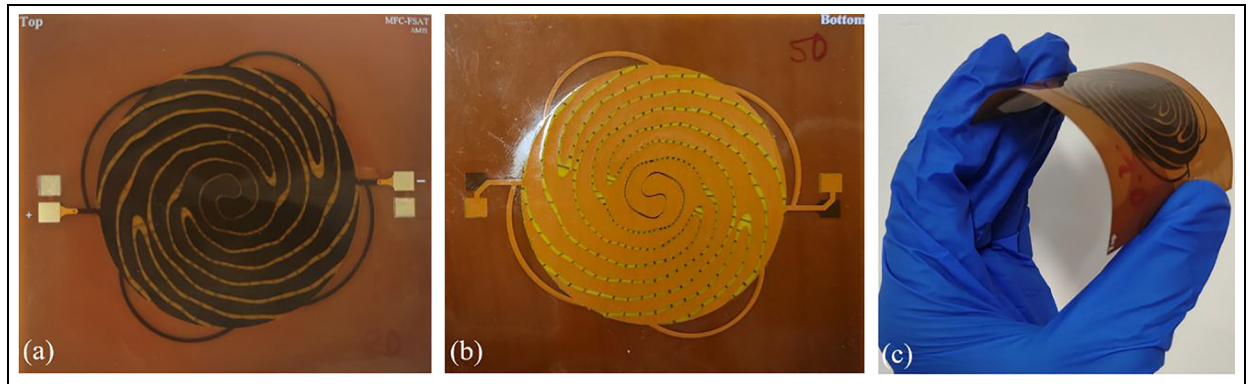


Figure 5. Transducer specimen: (a) top view, (b) bottom view, and (c) flexibility.

the domain. As a result, the patch is divided into two regions with opposite polarities, forming a two-channel transducer shape, as shown in Figure 4(c).

Configuration of the transducer

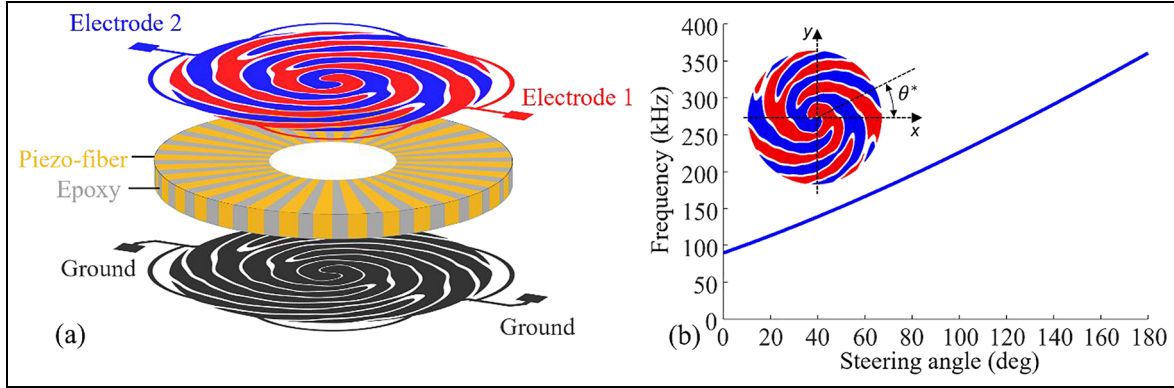
The PC-FSAT leverages the coupling between frequency and wavelength, while integrating the design principles of macro fiber composites.³⁰ It consists of an active piezoelectric fiber layer encapsulated between two thin flexible printed circuits which provides electrical channeling, mechanical support, and environmental protection. This laminated configuration enhances fracture toughness compared to monolithic piezoceramics by embedding the flexible fibers within a compliant epoxy matrix, which arrests crack propagation. Furthermore, the electrode configuration enables precise distinction of guided wave propagation directionality.

Within the active layer, piezoceramic fibers (PZT-5H; Wuxi City Huifeng Electronic Co., Ltd., Wuxi, Jiangsu, China) were arranged radially within an epoxy matrix (SWANCOR 2551; Tianjin Swancor Wind Power Materials Co., Ltd., Tianjin, China) selected for appropriate processing viscosity, strong adhesion, and favorable acoustic impedance. The layer was fabricated from bulk piezoceramic wafers, precisely machined into radial fibers using a computer-controlled dicing saw. This method not only optimized the transducer's cost-effectiveness but also allowed for enhancing directional sensitivity through the radial arrangement of the fibers, which maximized the piezoelectric coupling coefficient in Equation (5) for radial sensing. Furthermore, this composite structure provided mechanical flexibility, enabling transducer conformance to curved surfaces as depicted in Figure 5(c).

The electrode layer played a critical role in the generation and control of the electric field. The top electrodes were designed with a spiral pattern to enable

Table 1. The specifications of transducer.

Diameter	Direction	Wavenumber	Bandwidth
50 mm	$[0^\circ, 180^\circ]$	$[620, 1360]$ rads/m	$[90, 360]$ kHz

**Figure 6.** (a) typical components of transducer and (b) corresponding frequency-angle map.**Table 2.** Electrical parameters of PC-FSAT.

Insulation resistance	Static capacitance	Experiential bandwidth	Resonant impedance
$10^{11} \Omega$	965 pF	$[96, 376]$ kHz	48 Ω

PC-FSAT: piezoelectric composite frequency steerable acoustic transducer.

frequency-based beam steering. The back electrodes provided the common ground connection, ensuring a stable electrical operation, as depicted in Figure 5(a) and (b). These electrode patterns were fabricated on flexible copper-clad Kapton substrates (polyimide film; Guangzhou Anhua Electronics Co., Ltd., Guangzhou, Guangdong, China) using standard photolithography and etching techniques. Copper metallization provided low electrical resistance for efficient low-loss signal transmission. The thinness of the copper and Kapton layers maintained overall device flexibility without compromising electrical functionality.

The key parameters of the transducer are summarized in Table 1 for completeness. To achieve frequency-based directivity over the angular range from 0° to 180° , the transducer was designed to operate within the wavenumber range of 620–1360 rads/m. This range ensured that the transducer can effectively receive impact-guided waves across the desired angular spectrum. Concurrently, this frequency range of 90–360 kHz was carefully chosen to minimize both computational and experimental burdens. The corresponding frequency-angle map in Figure 6(b) is derived from

the dispersion analysis outlined in Figure 3, which characterizes the relationship between frequency with the steering angle.

To evaluate the electrical properties of the PC-FSAT, a series of tests were conducted using the impedance analyzer (Omicron Bode 100). It allowed for the precise measurement of impedance over a wide frequency range, enabling the characterization of key electrical properties of the transducer as shown in Table 2. Figure 7 displays the impedance curve of the proposed PC-FSAT, where the PC-FSAT was bonded on an aluminum plate. The spectrum validated that the transducer operated within the intended design bandwidth.

For further clarification of the performance, a comparison of sensing amplitude patterns from simulations at two different frequencies, 140 and 280 kHz, is presented in Figure 8. The directionality of guided wave control at the specified frequency aligned with the insights derived from the frequency-angle map, validating the design of the transducer and its ability to sense wave propagation effectively across the specified frequency range. This formed the foundation for the subsequent use of the transducers in impact localization.

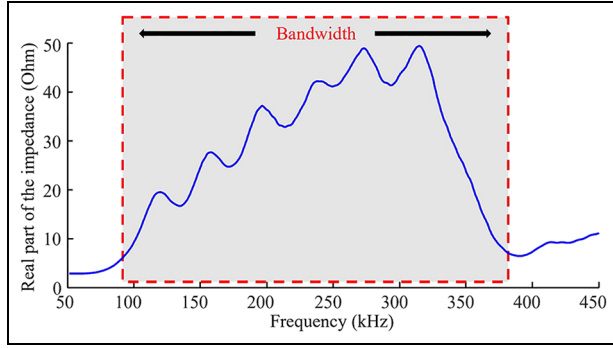


Figure 7. Measured impedance spectrum of a bonded PC-FSAT.

PC-FSAT: piezoelectric composite frequency steerable acoustic transducer.

Numerical modeling of PC-FSATs for impact monitoring

This section begins with the presentation of the FE model for the proposed impact monitoring system, designed to capture the system's response under impact excitations. Following this, the impact simulation is discussed, with particular emphasis on the propagation of guided waves during impact and the effectiveness of transducer-based localization.

The impact monitoring system model

A three-dimensional FE model of the impact system was created using COMSOL Multiphysics. The propagation medium was modeled as a 600×600 mm aluminum plate with a thickness of 1 mm. A transducer pair was modeled using piezoelectric materials, measuring 56 mm in diameter and 0.2 mm in thickness. As illustrated in Figure 9, the spiral electrode geometry

was implemented in the top and bottom of the piezoelectric material. The polarization direction of the piezoelectric element was assumed to be along the z -axis. It was essential to emphasize that the piezoelectric fibers were derived from a single, monolithic Lead Zirconate Titanate Type 5H (PZT-5H) piezoelectric ceramic. The homogenized parameters utilized in the simulation were calculated from the Voigt's model through the materials properties of PZT-5H and epoxy.^{31,32} The stiffness matrix $[C_P]$, piezoelectric matrix $[e_P]$, and dielectric matrix $[\epsilon_P]$, were calibrated in accordance with the adjustments proposed in Berger et al.,³³ in order to align with the unique characteristics of the fiber's radial orientation. The bonding scheme between the transducer and the aluminum plate was specified as a $30 \mu\text{m}$ thick epoxy glue layer.²⁸ Table 3 demonstrates the elastic and piezoelectric properties of the materials, including the drop-ball, aluminum plate, glue layer, and transducer. To account for the mechanical dissipation in the piezoelectric material, a mechanical damping was implemented using an Isotropic Loss Factor (η_s) of 0.006, based on a Mechanical Quality Factor (Q_m) of 80, as suggested by prior case studies.²⁶ This damping factor reflected the energy loss due to internal friction within the piezoelectric material during wave propagation, which was essential for accurately modeling the transducer's response to real-world conditions.

For impact detection, a drop ball model was used to simulate the impact event. The ball had a diameter of 5 mm and an initial velocity of 10 m/s, which corresponded to typical conditions for impact testing in similar applications. The time step in transient analysis was set to $0.1 \mu\text{s}$, ensuring that the analysis was sufficiently refined to capture the high-frequency components of guided waves, particularly within the

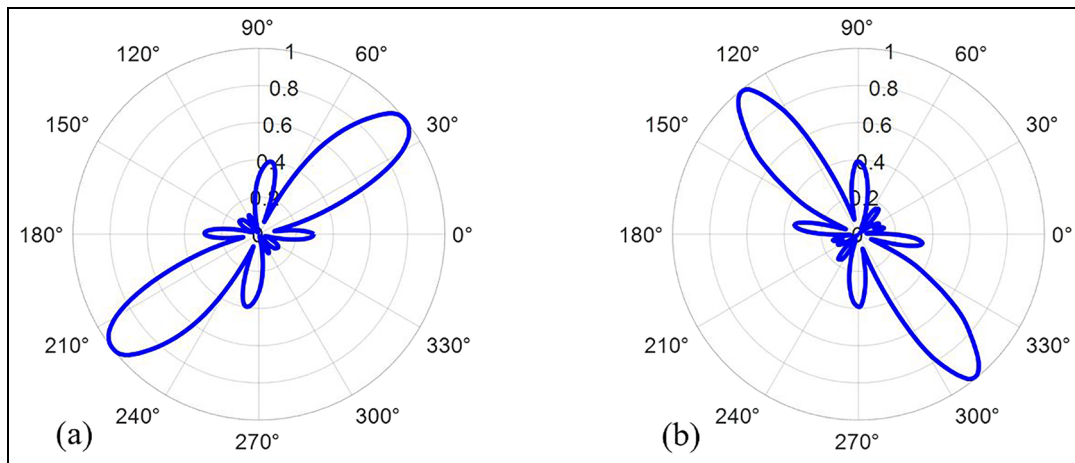


Figure 8. Normalized sensing amplitude patterns: (a) 140 kHz@40° and (b) 280 kHz@130°.

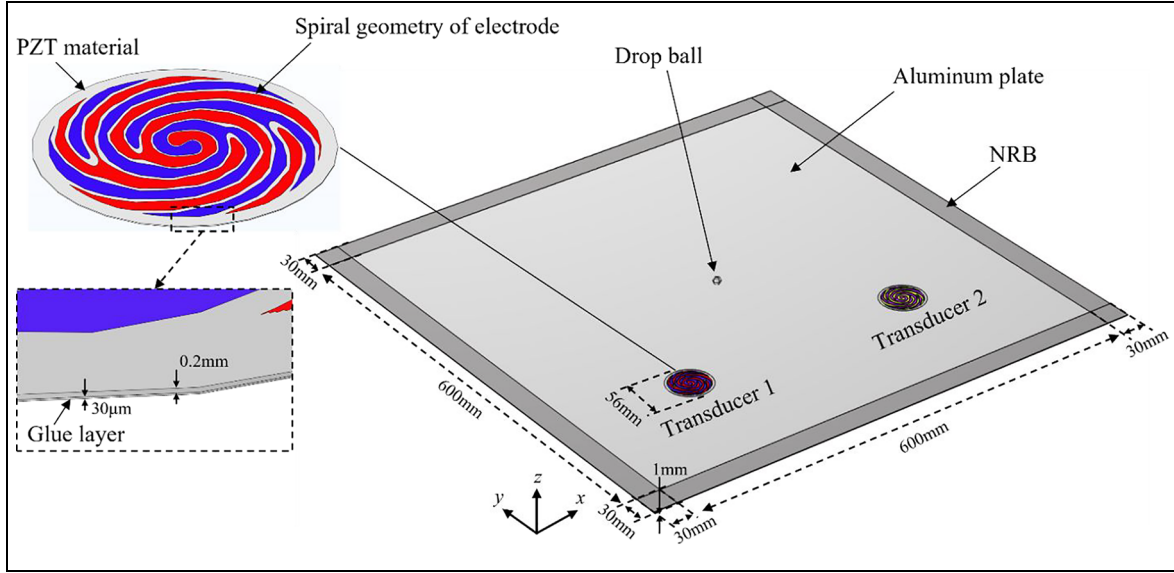


Figure 9. Three-dimensional geometry of the model in impact monitoring simulation.

Table 3. Elastic and piezoelectric properties of the materials in the simulation.

Property	Aluminum and drop-ball	Glue layer	Transducer materials
Density, ρ [kg/m ³]	2700	1150	5610
Elastic modulus, E [Gpa]	70	4.7	$C_{11} = C_{22} = 90.9686$ $C_{12} = 57.3697$ $C_{13} = C_{23} = 60.5547$ $C_{33} = 84.1086$ $C_{44} = C_{55} = 16.4144$ $C_{66} = 16.7995$
Poisson ratio	0.33	0.35	—
Piezoelectric constants, e [C/m ²]	—	—	$e_{31} = -4.6360$ $e_{33} = 16.2682$ $e_{15} = 11.9242$
Electrical permittivity, ϵ_{ijk}	—	—	$\epsilon_{11} = \epsilon_{22} = 1194.3$ $\epsilon_{33} = 1004.7$

operational frequency range of the transducer. To mitigate wave reflections at the boundaries of the simulation domain, non-reflective boundary (NRB) conditions were applied along all four edges of the plate, each extending 30 mm. This approach utilized a progressively increasing damping mechanism, which effectively absorbed the impact-generated waves before they reached the boundaries for simulating an unbounded domain for wave propagation. This technique was crucial for preserving the authenticity of the wave dynamics, ensuring that the results were not affected by boundary effects.

For the numerical meshing procedure, the transducer and aluminum plate were meshed with Free Triangular elements. Figure 10(b) and (d) illustrated

the resulting mesh of the transducers. A zoom-in view of the mesh is also provided. These figures highlighted the mesh density and element distribution, particularly the refinement in critical regions. To reduce the computational complexity, a swept mesh in the z -direction was employed for the plate. The mesh size was determined to be 10 times smaller than the shortest possible wavelength of the A_0 mode in the aluminum plate, as recommended by Ghose et al.³⁴ The in-plane mesh sizes of 0.5 and 1 mm were respectively employed for the transducer and the aluminum plate. The mesh sizes in z direction of the transducer and aluminum plate were 0.1 and 0.5 mm, respectively, reflecting a refined discretization for enhanced precision. Notably, the NRB domains were meshed using a swept grid

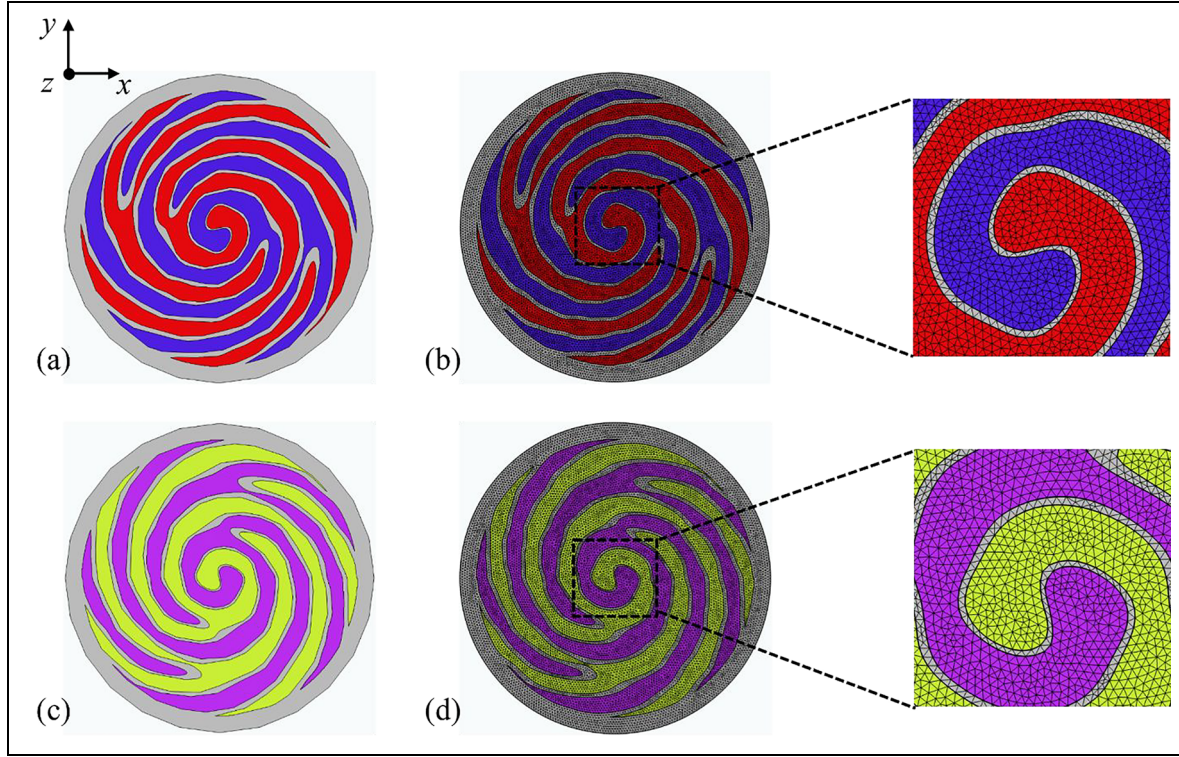


Figure 10. Transducer layout diagram: (a) PC-FSAT #1, (b) mesh detail of the PC-FSAT #1, (c) PC-FSAT #2 (90° counterclockwise rotation), and (d) mesh detail of the PC-FSAT #2.

PC-FSAT: piezoelectric composite frequency steerable acoustic transducer.

technique, with a mesh size of 1 mm to ensure optimal element quality and lowest computational burden.

To accurately model impacts from various orientations with respect to PC-FSATs, simulations were conducted using aluminum balls dropped onto aluminum plates at different locations. The resulting scenarios can be represented by two distinct impact models as illustrated in Figure 11. One significant challenge identified in the study was the inherent limitations of transducer directivity due to its size and design constraints. Specifically, it was observed that when the impact direction exceeded 90°, the transducer could no longer maintain a well-defined directivity for receiving guided waves. Instead, it was affected by sidelobes, leading to misjudgment in frequency spectral capture. This resulted in a reduction in signal accuracy, thereby weakening the ability to precisely detect the impact point. To address this issue, a more reliable arrangement was designed to improve the detection accuracy and ensure efficient usage of transducer. As illustrated in Figure 10(c), the second transducer was rotated 90° counterclockwise relative to the first one. This rotation allowed the two transducers most accurate range to face the monitoring area.

Table 4 presents the impact position information and the corresponding frequencies. In case 1, the impact point was aligned with the 45° line of the transducer arrangement. As a result of the setup's symmetry, both transducers received signals with identical theoretical frequencies. This case represented an ideal scenario where the impact point was perfectly positioned at the center of the plate. In contrast, case 2 introduced variability by placing the impact point at an arbitrary angle. In this case, the received signals from the two transducers differed, resulting in distinct frequency values. This scenario illustrated the effect of random impact angles on signal reception, resulting in differences in the measured frequencies.

Simulation results and signal processing for impact localization

A transient pulse is generated when a mechanical impact occurs on the surface of a structure, initiating an acoustic wave that propagates through the material in spherical wavefronts. Figure 12 illustrates the generation of guided waves at the impact location and their propagation toward the transducers. A key

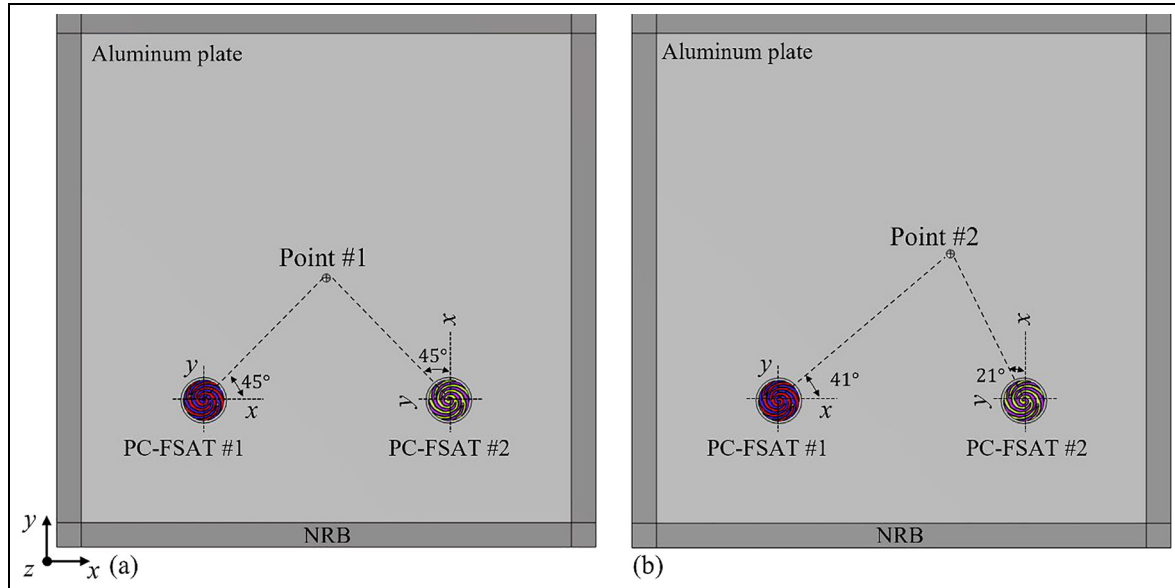


Figure 11. Case studies for the impact monitoring: (a) case 1 and (b) case 2.

Table 4. Impact point information and corresponding frequency for simulation.

Case	Transducer	Simulated impact point	Steering angle	Frequency
Case 1	PC-FSAT #1	X: 330 mm, Y: 330 mm	45°	146 kHz
	PC-FSAT #2		45°	146 kHz
Case 2	PC-FSAT #1	X: 390 mm, Y: 360 mm	41°	140 kHz
	PC-FSAT #2		21°	122 kHz

PC-FSAT: piezoelectric composite frequency steerable acoustic transducer.

observation was that the excited guided wave contained a wide frequency spectrum. The leading waves exhibited shorter wavelengths with higher frequencies, while the subsequent waves displayed progressively longer wavelengths with lower frequencies. Additionally, Figure 12 also emphasizes the role of the NRB in effectively absorbing the guided waves. The guided waves propagated without noticeable reflections at the boundary, thereby confirming the efficacy of the implemented NRB conditions in effectively mitigating edge-induced interference.

The guided wave signal generated by impact pulse excitation is inherently broadband, encompassing a wide range of frequencies, as is evident in Figure 13, which also illustrates the signal processing procedure. Through this process, redundant signal components were removed, allowing for the isolation of key features of interest. Figure 13(a) illustrates the received raw time-domain impact signal, with the focus of this study being on the guided wave component that first reaches the transducer. Consequently, the complete

time-domain impact signal was not acquired. This approach not only substantially reduced the computational burden in the simulation but also effectively mitigated interference from reflected waves in practice. It should be noted that the high-amplitude tail signal represents the dispersive, low-frequency, low-speed A_0 wave component. It will eventually reach zero, given sufficiently long time for signal acquisition. Figure 13(b) depicts the corresponding frequency-domain representation, which exhibits notable distinctions from the impact response of conventional piezoelectric wafer active sensors on aluminum plates. The spectral trend observed in this study originated from the distinctive spectral response characteristics of PC-FSAT. Ideally, the frequency-domain representation of the received signal should exhibit a pronounced response at the transducer's sensitive frequencies, effectively correlating with the directional attributes of the impact event. However, due to practical constraints related to physical dimensions during the manufacturing and design processes, the number of repeated electrode pattern fell

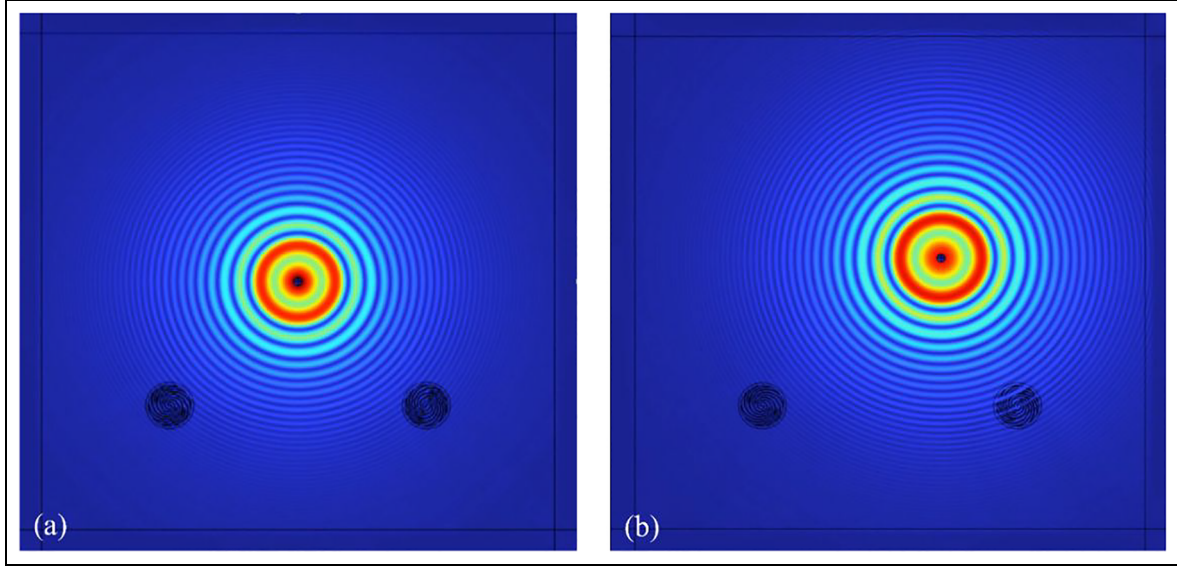


Figure 12. Snapshots of impact stress wavefields: (a) case 1 and (b) case 2.

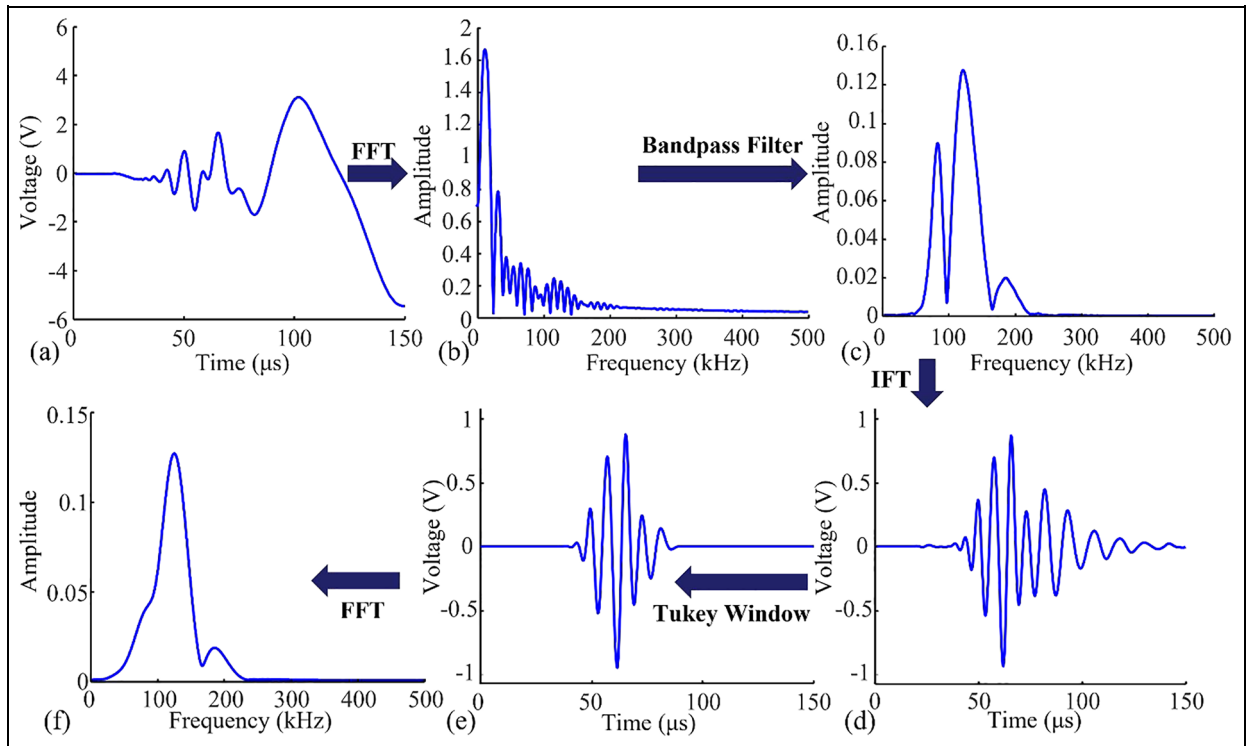


Figure 13. Signal processing procedure: (a) original temporal signal, (b) original signal spectrum, (c) spectrum after Butterworth bandpass filtering, (d) temporal signal via IFT, (e) temporal signal after Tukey window filtering, and (f) final spectral response. IFT: inverse Fourier transform.

short of the optimal configuration, resulting in fluctuations across the frequency spectrum. It would not impede the efficacy of subsequent signal processing or the precision of impact localization. The initial step in

signal processing applies a fifth-order Butterworth bandpass filter, with a cut-off frequency range set between 80 and 220 kHz (half of the transducer's frequency band). The primary goal of this filtering

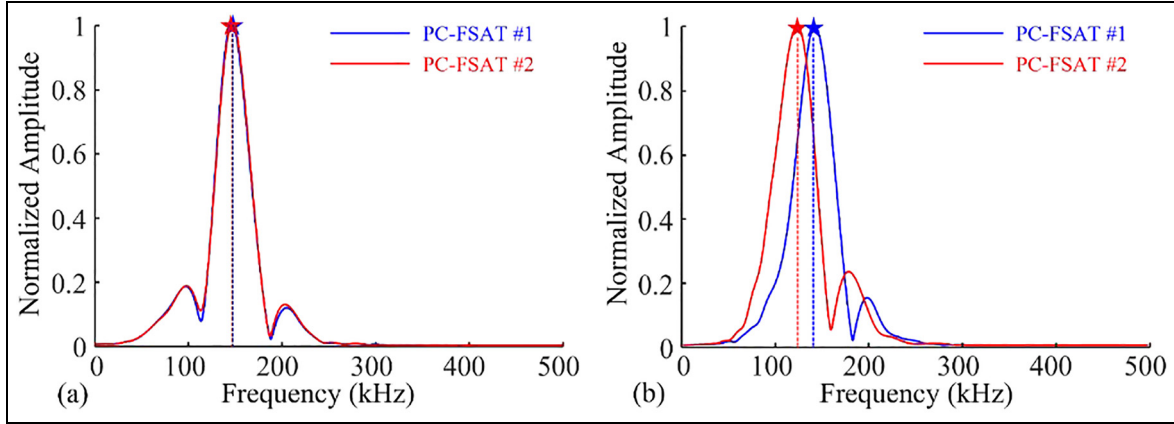


Figure 14. Spectral response after signal processing: (a) case 1 and (b) case 2.

operation was to eliminate both low-frequency noise and high-frequency components that could obscure the desired signal. This bandpass filter ensured that only the frequencies relevant to the guided waves were preserved. In addition to this frequency-domain filtering, the temporal signal was further refined by applying a Tukey window function. This windowing technique was specifically designed to obtain the main wave packet of the guided wave ensuring that the signal's most significant components were retained. Such an operation also ensures that any reflections could be removed in practical cases. Through these combined spectral and temporal processing, a high degree of signal purity and consistency could be achieved. The carefully processed signal, free from extraneous noise and irrelevant components, provided valuable insights for impact monitoring and facilitated precise impact localization.

By analyzing the frequency components of the final signals, the orientation of the incident wave resulting from the impact could be assessed. Figure 14 presents the normalized frequency-domain representations of the final signals. Vertical dashed lines marked the center frequencies of the spectra, which allowed a direct visual comparison of the prediction accuracy. The center frequencies aligned closely with the theoretical design values provided in Table 4, further confirming the accuracy of the system. The results indicated that while the applied filtering strategy led to a slight reduction in signal richness, it would not diminish the effectiveness of the transducer.

The location of the impact event is determined by the intersection of the test angles of the two transducers, as shown in Figure 15. The results for both test cases were presented in Table 5, where the calculated impact positions were compared to the simulated impact locations. A quantitative analysis on the error

of impact location was conducted. The mathematical formula for the index is given in the following expression:

$$\text{Error} = \frac{\sqrt{(X - X_1)^2 + (Y - Y_1)^2}}{L} \quad (11)$$

where (X, Y) represents the calculated impact location, while (X_1, Y_1) corresponds to the simulated impact location. The L denotes the length of the aluminum plate. The errors between the calculated and simulated locations were found to be within 1%, suggesting that the method was highly accurate. This low error margin highlighted the effectiveness of the angular intersection technique in determining the impact location. The consistency between the calculated and predicted positions further supported the reliability of the sensing system. Despite the slight variation between the two cases, the overall accuracy remained robust, confirming the practical applicability of the approach.

Experimental demonstration for impact monitoring

To verify the performance and accuracy of the monitoring system, a series of controlled impact experiments were conducted on a square aluminum plate with dimensions of 800 mm in length, 800 mm in width, and 1 mm in thickness. The experimental setup is comprised of an NI PXIe-1071 high-performance data acquisition device and a three-degree-of-freedom drop ball platform, as shown in Figure 16. The data acquisition device played a critical role in both signal acquisition and post-processing tasks, capturing high-fidelity data for further analysis. The aluminum plate was supported at all four corners and positioned to

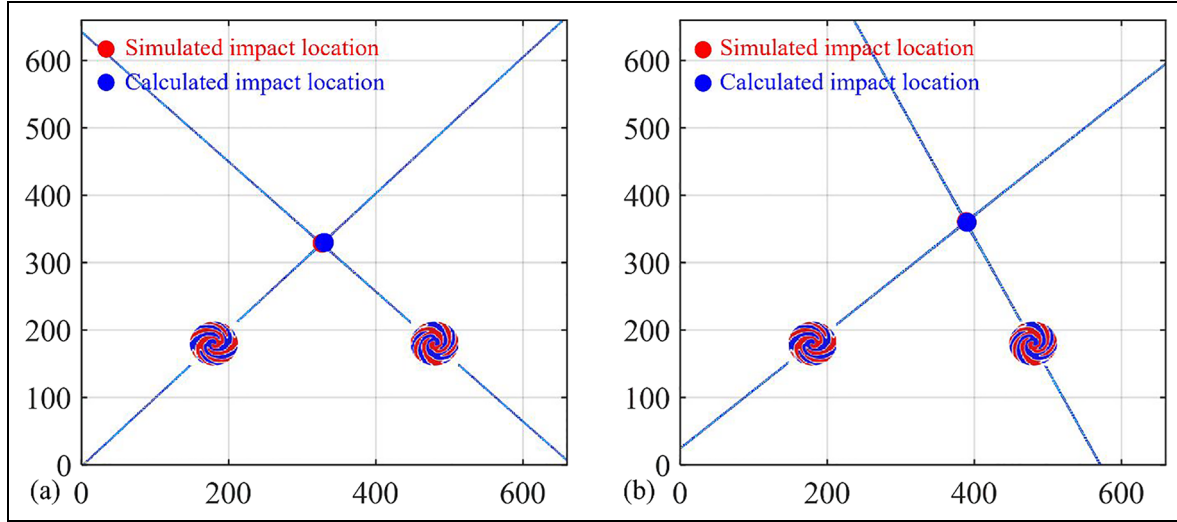


Figure 15. Impact localization results: (a) case 1 and (b) case 2.

Table 5. The monitoring impact point information.

Case	Transducer	Frequency-angle	Calculated impact location	Error (%)
Case 1	PC-FSAT #1	146 kHz–45.32°	X_I : 327 mm, Y_I : 329 mm	0.53
	PC-FSAT #2	147 kHz–46.07°		
Case 2	PC-FSAT #1	140 kHz–40.84°	X_I : 389 mm, Y_I : 361 mm	0.24
	PC-FSAT #2	122 kHz–116.92°		

PC-FSAT: piezoelectric composite frequency steerable acoustic transducer.

simulate the free boundary conditions used in the simulation. The transducers were carefully placed at two fixed locations: point 1 at coordinates (150, 200) and point 2 at (650, 200), assuring a sufficiently large detection area. Signal acquisition was initiated using a LabVIEW program that triggered data recording once the impact-generated voltage surpassed a predefined threshold, ensuring the system to capture the relevant signals without recording unnecessary noise from background activities. The triggering mechanism was fine-tuned to initiate signal acquisition when the impact signal reached 20% of its maximum value. This adjustment helped prevent false alarms during the impact process, while maintaining a rapid response time to capture the transient signals of the impact event.

The impact was created by a drop ball, with its position and height precisely controlled using a slide rail system. This system allowed movement along both the parallel and perpendicular axes relative to the plate, covering a working dimension of $1.2 \times 1.2 \times 1$ m. It provided comprehensive spatial coverage, ensuring that the ball could be dropped at multiple locations to generate the impact events on the plate. An *L*-shaped metal block was fixed to the *z*-axis screw of the slider

with an electromagnet attached to the block, which had a maximum holding force of 100 N. It was used to keep the ball suspended at a precise height until the power was cut off, allowing the ball to fall freely. This mechanism ensured that the ball was released from a consistent height and position for each experiment. The ability to adjust both the position and the height of the ball allowed for the simulation of impact events at various locations on the plate with different energy levels. As the ball fell and impacted the plate, the corresponding guided wave signals generated by the impact was recorded by the sensing system.

Figure 17 illustrates the processing of the actual impact signals. The experimental temporal signals closely matched the simulation results, exhibiting prominent high-frequency components in the beginning and low-frequency contents in the coda signal. Spectral analysis revealed that the primary frequency components of the signal concentrated in the lower frequency range. This frequency range was far away from the transducer's effective operational bandwidth (90–360 kHz). It should be noted that, in this experiment, absorbing boundary conditions were not applied, in alignment with typical real-world applications. After

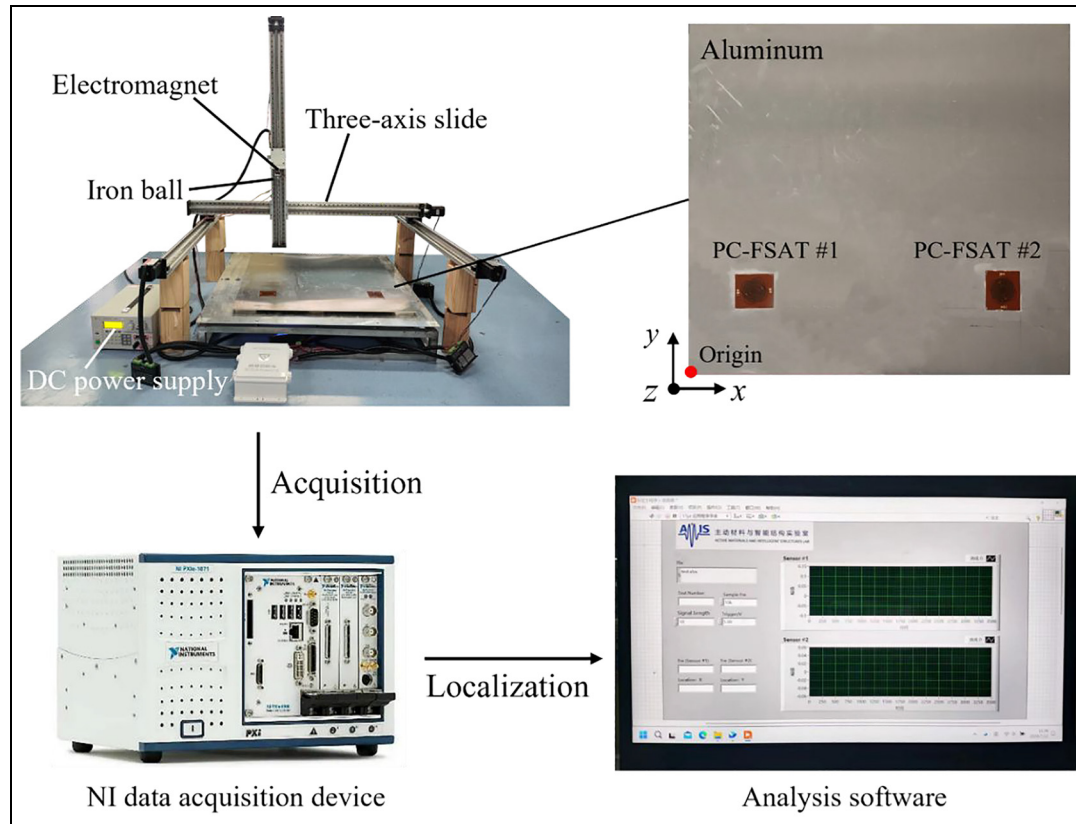


Figure 16. Experimental setup of the impact monitoring system.

Table 6. The monitoring impact point information and comparison results.

Case	Actual impact location	Calculated impact location (mean value)
Case 1	X: 400 mm, Y: 400 mm	X_i : 399 mm, Y_i : 416 mm
Case 2	X: 200 mm, Y: 300 mm	X_i : 212 mm, Y_i : 338 mm
Case 3	X: 200 mm, Y: 400 mm	X_i : 213 mm, Y_i : 380 mm
Case 4	X: 200 mm, Y: 500 mm	X_i : 199 mm, Y_i : 529 mm
Case 5	X: 600 mm, Y: 300 mm	X_i : 591 mm, Y_i : 348 mm
Case 6	X: 600 mm, Y: 400 mm	X_i : 540 mm, Y_i : 418 mm
Case 7	X: 600 mm, Y: 500 mm	X_i : 551 mm, Y_i : 487 mm

filtering, the temporal signal as shown in Figure 17(d) displayed the phenomenon of multiple overlapping wave packets. The time-domain window effectively isolated the first-arriving ultrasonic guided wave packet, while diminishing the influence from subsequent reflections. This technique ensured that only the relevant signal was captured and analyzed, enhancing signal feature identification accuracy. By performing spectral analysis on the isolated wave packet, a clean and distinct frequency response could be obtained as shown in Figure 17(f). This process mitigated the frequency aliasing, allowing for more precise and reliable localization of the impact event. In the following case study, a

series of impact events were systematically investigated and analyzed. Figure 17(a) illustrates the distribution of the impact events, with the specific coordinates provided in Table 6. These points represented the locations of impact points, where the ball was controlled to fall freely from the same height at each point and struck the platform surface with 0.7 J of energy. To achieve statistical validity, 100 experiments were repeated for each designated impact point. This extensive replication improved data reliability. By averaging the results, a statistical understanding of accuracy and variability can be developed, leading to a more comprehensive evaluation of the proposed monitoring method.

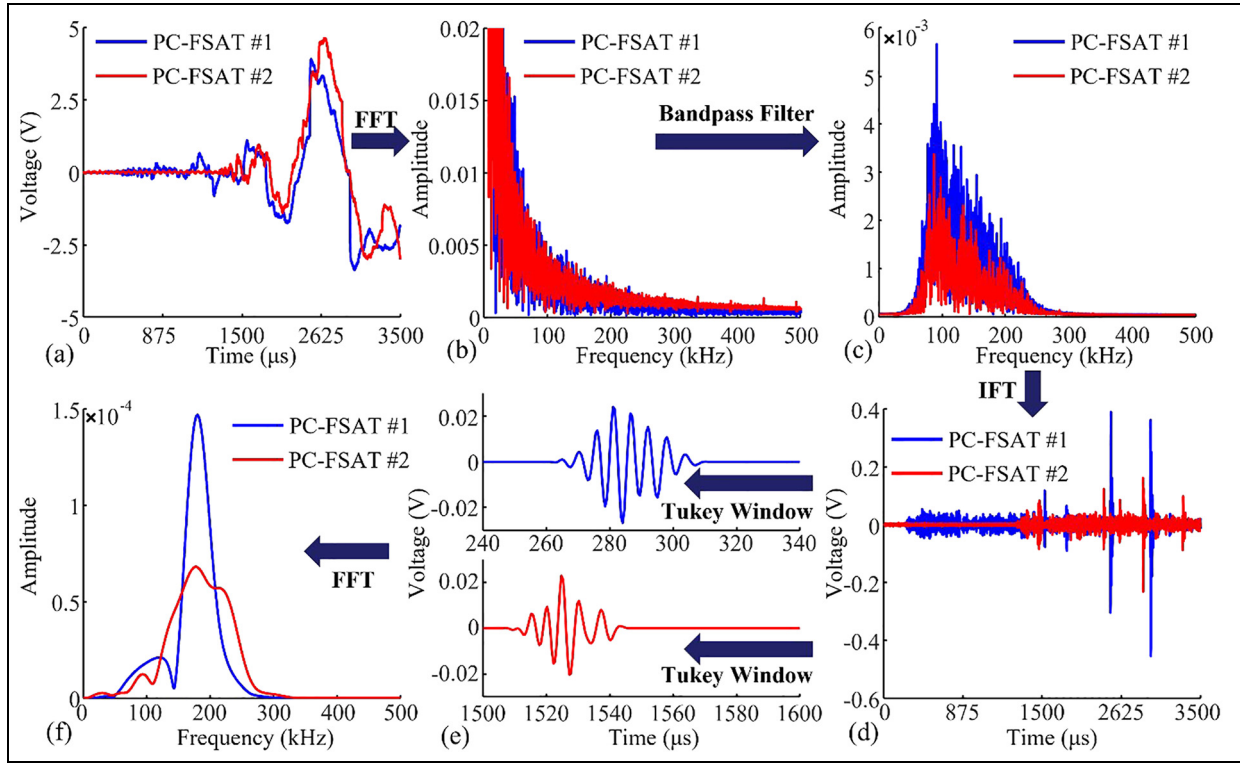


Figure 17. Signal processing procedure: (a) original temporal impact signal, (b) signal spectra, (c) spectra after Butterworth bandpass filtering, (d) temporal signal via IFT, (e) temporal signal after Tukey window filtering, and (f) final frequency response. IFT: inverse Fourier transform.

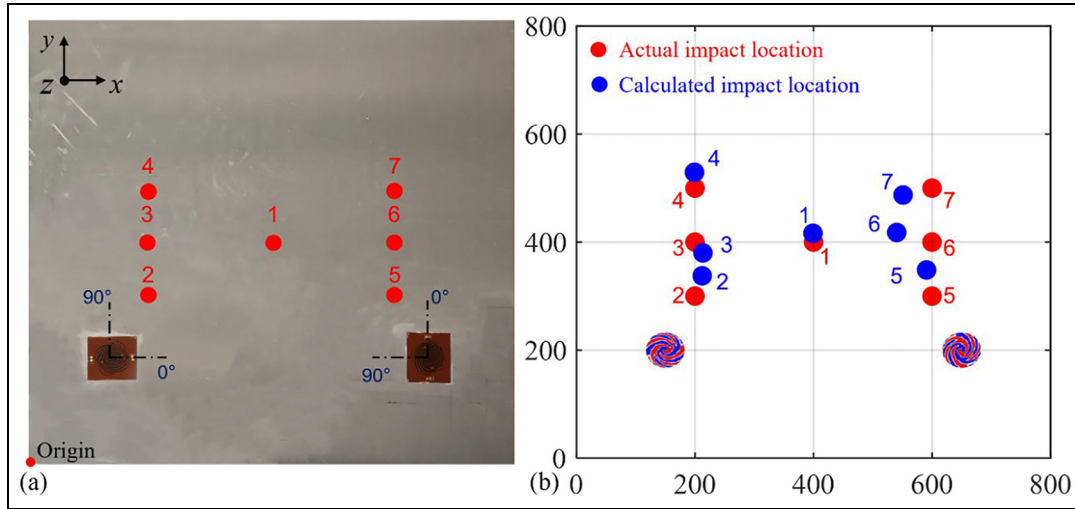


Figure 18. Impact localization: (a) impact events and (b) monitoring results.

The comparison between the actual impact locations and the calculated monitoring locations is shown in Figure 18(b). The majority of the monitored impact locations showed good alignments with the actual impact coordinates, indicating that the system

effectively evaluated and monitored the impact events, as detailed in Table 6. Figure 19 illustrates the calculated mean error and error variance for each impact point. Most of the impact points had errors smaller than 5%, while a few points displayed more significant

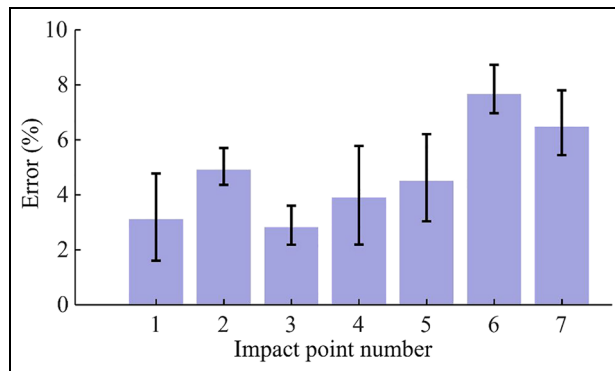


Figure 19. Errors of the impact results.

deviations, particularly those near the edges of the plate and far away from the transducers, such as point 6 and point 7. The larger errors could be caused by several factors. Firstly, the limited size of the impact plate in the laboratory setup was likely a significant factor. For impact points near the edges of the plate, reflection signals may affect the sensing signals. In these regions, multiple reflections and signal overlaps likely occurred, resulting in signal interferences. Secondly, the transducer bonding quality may also contribute to the observed monitoring errors. When the impact point was too close to the limited angle and far away from the transducer, the sensitivity and response characteristics were compromised, leading to measurement discrepancies. In future applications, the placement of transducers should be optimized to address these limitations.

Conclusion and future work

This paper presented a novel approach for impact monitoring through the development of PC-FSATs. The proposed transducers leveraged frequency-dependent beaming for directional sensing of guided waves, significantly simplifying impact detection systems by reducing the need for dense sensor networks. By embedding radially orientated piezoceramic fibers into flexible printed circuits, the transducers combined high directional sensitivity with enhanced flexibility. Both numerical and experimental results demonstrated that the PC-FSATs accurately detected and localized impacts with high precision, offering a cost-effective and reliable solution for impact monitoring.

Future research will focus on refining the transducer design for even better performance in diverse structures and environments. The adaptability of the transducers to anisotropic composite structures should be carried out.

Declaration of conflicting interests


The author(s) declared no potential conflicts of interest with respect to the research, authorship, and/or publication of this article.

Funding

The author(s) disclosed receipt of the following financial support for the research, authorship, and/or publication of this article: The support from the National Natural Science Foundation of China (contract number 52475161) is thankfully acknowledged. Dr. Yanfeng Shen appreciates the funding from John Wu & Jane Sun Endowed Professorship.

ORCID iDs

Shulong Zhou  <https://orcid.org/0000-0003-1663-0018>

Yanfeng Shen  <https://orcid.org/0000-0002-3025-4664>

References

- Giurgiutiu V, Zagari A and Jing Bao J. Piezoelectric wafer embedded active sensors for aging aircraft structural health monitoring. *Struct Health Monit* 2002; 1(1): 41–61.
- Ihn J-B and F.-Chang K. Detection and monitoring of hidden fatigue crack growth using a built-in piezoelectric sensor/actuator network: I. Diagnostics. *Smart Mater Struct* 2004; 13(3): 609–620.
- Hajzargerbashi T, Kundu T and Bland S. An improved algorithm for detecting point of impact in anisotropic inhomogeneous plates. *Ultrasonics* 2011; 51(3): 317–324.
- Mesnil O, Leckey CA and Ruzzene M. Instantaneous and local wavenumber estimations for damage quantification in composites. *Struct Health Monit* 2015; 14(3): 193–204.
- Ren Y, Qiu L, Yuan S, et al. A diagnostic imaging approach for online characterization of multi-impact in aircraft composite structures based on a scanning spatial-wavenumber filter of guided wave. *Mech Syst Signal Process* 2017; 90: 44–63.
- Yuan S, Chen J, Yang W, et al. On-line crack prognosis in attachment lug using Lamb wave-deterministic resampling particle filter-based method. *Smart Mater Struct* 2017; 26(8): 085016.
- Sikdar S, Kudela P, Radziński M, et al. Online detection of barely visible low-speed impact damage in 3D-core sandwich composite structure. *Compos Struct* 2018; 185: 646–655.
- Wang Y, Qiu L, Luo Y, et al. A stretchable and large-scale guided wave sensor network for aircraft smart skin of structural health monitoring. *Struct Health Monit* 2021; 20(3): 861–876.
- Faisal Haider M, Migot A, Bhuiyan MY, et al. Experimental investigation of impact localization in composite plate using newly developed imaging method. *Inventions* 2018; 3(3): 59.
- Giridhara G, Rathod VT, Naik S, et al. Rapid localization of damage using a circular sensor array and Lamb

- wave based triangulation. *Mech Syst Signal Process* 2010; 24(8): 2929–2946.
11. Yuan S, Ren Y, Qiu L, et al. A multi-response-based wireless impact monitoring network for aircraft composite structures. *IEEE Trans Ind Electron* 2016; 63(12): 7712–7722.
 12. Bulletti A, Merlo EM and Capineri L. Analysis of the accuracy in impact localization using piezoelectric sensors for Structural Health Monitoring with multichannel real-time electronics. In: *2020 IEEE 7th international workshop on metrology for AeroSpace (MetroAeroSpace)*, Pisa, Italy, Jun. 2020, pp. 480–484. IEEE.
 13. Zheng F and Yuan S. Research on composite impact localization by MUSIC based guided wave monitoring. In: *2022 IEEE international conference on prognostics and health management (ICPHM)*, Detroit (Romulus), MI, USA, Jun. 2022, pp. 154–160. IEEE.
 14. Feng B, Cheng S, Deng K, et al. Localization of low-velocity impact in CFRP plate using time–frequency features of guided wave and convolutional neural network. *Wave Motion* 2023; 119: 103127.
 15. Zhu C, Xu Z, Huang Y, et al. Flexible, monolithic piezoelectric sensors for large-area structural impact monitoring via MUSIC-assisted machine learning. *Struct Health Monit* 2024; 23(1): 121–136.
 16. Matt H and Lanza Di Scalea F. Macro-fiber composite piezoelectric rosettes for acoustic source location in complex structures. In: Tomizuka M, Yun C-B and Giurgiutiu V (ed.) *The 14th international symposium on: smart structures and materials & nondestructive evaluation and health monitoring*, San Diego, CA, USA, 2007, p. 65290Q.
 17. Laude V, Gérard D, Khelifaoui N, et al. Subwavelength focusing of surface acoustic waves generated by an annular interdigital transducer. *Appl Phys Lett* 2008; 92(9): 094104.
 18. Wang C, Wang Z, Ren T-L, et al. A micromachined piezoelectric ultrasonic transducer operating in d33 mode using square interdigital electrodes. *IEEE Sens J* 2007; 7(7): 967–976.
 19. Romanoni M, Apetre N, Ruzzene M, et al. Two-dimensional periodic actuators for frequency-based beam steering. Presented at the *SPIE smart structures and materials + nondestructive evaluation and health monitoring*, Kundu T (ed.), San Diego, CA, USA, 2009, p. 729526.
 20. Senesi M, Xu B and Ruzzene M. Experimental characterization of periodic frequency-steerable arrays for structural health monitoring. *Smart Mater Struct* 2010; 19(5): 055026.
 21. Baravelli E, De Marchi L, Ruzzene M, et al. Photolithography-based realization of frequency steerable acoustic sensors on PVDF substrate. In: *2012 IEEE sensors applications symposium proceedings*, Brescia, Italy, Feb. 2012, pp. 1–6. IEEE.
 22. Senesi M and Ruzzene M. A frequency selective acoustic transducer for directional lamb wave sensing. *J Acoust Soc Am* 2011; 130(4): 1899–1907.
 23. Senesi M, Baravelli E, De Marchi L, et al. Experimental demonstration of directional GW generation through wavenumber-spiral frequency steerable acoustic actuators. In: *2012 IEEE international ultrasonics symposium*, Dresden, Germany, 2012, pp. 2694–2697. IEEE.
 24. Senesi M and Ruzzene M. A spiral frequency steerable acoustic transducer for SHM. In: Tomizuka M (ed.) *SPIE smart structures and materials + nondestructive evaluation and health monitoring*, San Diego, CA, USA, 2011, p. 798136.
 25. Monkhouse RSC, Wilcox PD and Cawley P. Flexible interdigital PVDF transducers for the generation of Lamb waves in structures. *Ultrasonics* 1997; 35(7): 489–498.
 26. Mohammadgholiha M, Palermo A, Testoni N, et al. Finite element modeling and experimental characterization of piezoceramic frequency steerable acoustic transducers. *IEEE Sens J* 2022; 22(14): 13958–13970.
 27. Dibiasi M, Mohammadgholiha M and De Marchi L. Optimal array design and directive sensors for guided waves DoA estimation. *Sensors* 2022; 22(3): 780.
 28. Mohammadgholiha M, Moll J, Tschöke K, et al. Unidirectional frequency-steerable acoustic transducer for guided ultrasonic wave damage imaging. *Mech Syst Signal Process* 2025; 229: 112505.
 29. Baravelli E, Senesi M, Ruzzene M, et al. Fabrication and characterization of a wavenumber-spiral frequency-steerable acoustic transducer for source localization in plate structures. *IEEE Trans Instrument Meas* 2013; 62(8): 2197–2204.
 30. Kim D and Philen M. On the Beamsteering Characteristics of MFC Phased Arrays for Structural Health Monitoring. In: *49th AIAA/ASME/ASCE/AHS/ASC structures, structural dynamics, and materials conference*, Schaumburg, IL, USA, 2008, p. 1969.
 31. Rianoyi R, Potong R, Jaitanong N, et al. Dielectric, ferroelectric and piezoelectric properties of 0-3 barium titanate–Portland cement composites. *Appl Phys A* 2011; 104(2): 661–666.
 32. Dong B and Li Z. Cement-based piezoelectric ceramic smart composites. *Compos Sci Technol* 2005; 65(9): 1363–1371.
 33. Berger H, Gabbert U, Köppe H, et al. Finite element analysis and design of piezoelectric controlled smart structures. *J Theoretical Appl Mech* 2000; 38(3): 475–498.
 34. Ghose B, Balasubramaniam K, Krishnamurthy CV, et al. Two dimensional FEM simulation of ultrasonic wave propagation in isotropic solid media using COMSOL. In: *COMSOL conference*, Bangalore, India, 2010, pp. 37–38.